A New Deep-Learning-Based Framework for Ice Water Path Retrieval From Microwave Humidity Sounder-II Aboard FengYun-3D Satellite

Wenyu Wang, *Member, IEEE*, Jian Xu, *Senior Member, IEEE*, Husi Letu, *Senior Member, IEEE*, Lanjie Zhang, *Member, IEEE*, Zhenzhan Wang, and Jiancheng Shi, *Fellow, IEEE*

***Abstract*— The derivation of ice water path (IWP) from microwave (MW) radiometer measurements is challenging. This study presents a deep learning framework for global retrieval of IWP using observations from the Microwave Humidity Sounder-II (MWHS-II) aboard the FengYun-3D (FY-3D) satellites. Two deep learning models, deep forest (DF21) and quantile regression neural network (QRNN), are constructed to detect ice cloud flags and retrieve IWP. By collocating MWHS-II observations with 2C-ICE, a joint product of CloudSat and Cloud-Aerosol Lidar and Infrared Pathfinder Satellite Observations (CALIPSO), deep learning models learn the characteristics of IWP from MWHS-II brightness temperatures (BTs). The test results show that the MWHS-II channels provide more information on IWP than the MWHS channels, particularly the 89-GHz channel and the 118-GHz channels with an offset of ≥0.8 GHz. Combining the QRNN and DF21 models, the IWP retrieval results in a root mean square error (RMSE) of 707.346 g/m^2, mean absolute percentage error (MAPE) of 65.122%, mean bias error (MBE) of −104 g/m^2, determination coefficient (R^2) of 0.683, and Pearson correlation coefficient (PCC) of 0.831. Application of the models to MWHS-II observations of tropical cyclone CILIDA shows better agreement with 2C-ICE. All the datasets exhibit a similar feature on the monthly mean scale, but the magnitudes of IWP differ. Compared with GMI-GPROF, MODIS, and ERA5 IWP products, MWHS-II results are closest to 2C-ICE. Similar results are also shown for the zonal mean data. These results show that deep learning methods efficiently and probabilistically retrieve IWP from long-term observation data of MWHS/MWHS-II.**

Manuscript received 21 September 2023; revised 13 December 2023 and 4 January 2024; accepted 8 January 2024. Date of publication 11 January 2024; date of current version 24 January 2024. This work was supported in part by the National Natural Science Foundation of China under Grant 42105130 and Grant 42241162, and in part by the Chinese Academy of Sciences (CAS) Pioneering Initiative Talents Program under Grant E1RC2WB2. *(Corresponding authors: Jian Xu; Husi Letu.)*

Wenyu Wang and Zhenzhan Wang are with the Key Laboratory of Microwave Remote Sensing, National Space Science Center, Chinese Academy of Sciences, Beijing 100190, China (e-mail: wangwenyu@nssc.ac.cn; wangzhenzhan@mirslab.cn).

Jian Xu and Jiancheng Shi are with the National Space Science Center, Chinese Academy of Sciences, Beijing 100190, China (e-mail: xujian@nssc.ac.cn; shijiancheng@nssc.ac.cn).

Husi Letu is with the Aerospace Information Research Institute, Chinese Academy of Sciences, Beijing 100101, China (e-mail: husiletuw@hotmail.com).

Lanjie Zhang is with the Key Laboratory of Information and Communication Systems, Ministry of Information Industry, Beijing Information Science and Technology University, Beijing 100101, China (e-mail: zhanglanjie@bistu.edu.cn).

Digital Object Identifier 10.1109/TGRS.2024.3352654

***Index Terms*— Deep learning, ice water path (IWP), microwave humidity sounder (MWHS).**

I. Introduction

THE importance of ice clouds and their impact on the Earth's climate system and global energy budget have already been emphasized [1], [2], [3]. Ice cloud measurement is a difficult problem of great concern to atmospheric science research for a long time. Since it is impractical to measure ice clouds in situ globally and ground-based instruments can only provide limited coverage data, spaceborne remote sensing provides an efficient way to observe global-scale ice clouds. Active radars provide better accuracy and higher spatial resolution while passive instruments are far superior in geographical coverage. In addition, the fact that different frequencies are sensitive to different ice particle sizes makes it possible for passive radiometers covering multiple frequency bands (from millimeter to submillimeter) to better measure ice clouds [4]. The Ice Cloud Imager (ICI) which will be launched aboard Metop Second Generation (Metop-SG B) satellite of the Earth Polar System Second Generation (EPS-SG) program at the end of 2025 and the similar instruments are proven to have comparable ice water path (IWP) accuracy to 94-GHz radar, and they can be combined to improve measurement capabilities [5], [6], [7], [8], [9].

To date, most passive microwave (MW) radiometers are limited to frequencies below 200 GHz, and only TROPICS Millimeter-wave Sounder (TMS) aboard Time-Resolved Observations of Precipitation structure and storm Intensity with a Constellation of Smallsats (TROPICS) launched in 2021 can provide measurement near 205 GHz which is more sensitive to precipitation-sized ice particles [10], [11]. The meteorological satellite Fengyun-3 (FY-3) is the second generation of polar-orbiting meteorological satellites in China, and the MicroWave Humidity Sounder-II (MWHS-II) aboard FengYun-3D (FY-3D) has similar channels from 89 to 190 GHz which are also sensitive to large ice particles (mostly snow particles) [12]. Given the measurement characteristics and global coverage provided by the instrument, robust algorithms for deriving ice cloud properties from MWHS-II would be highly desirable.

Machine learning (ML) approaches can extract nonlinear relationships between the measurements and parameters of

interest without assumptions in physical models. It has indicated the immense potential for solving complex inverse problems which is not easily solved by conventional physics-based methods. The deep learning method is an alternative, efficient, and easy-to-use approach that has already been widely used in the area of meteorological element retrieval. There are pros and cons in both the methods. Physics-based algorithms have clearer physical mechanisms and processes to analyze the sources of retrieval error and have been well used in atmospheric temperature, humidity, and atmospheric composition products, but there is a problem of high computational complexity and low accuracy in complex physical processes such as ice clouds. On the contrary, deep learning has the advantage of being computationally fast and relatively more accurate in complex physics problems, but it has the disadvantage of relying heavily on real data and the inability to trace physical processes back to their source, so it is not suitable for all problems. Numerous researches have been conducted to use ML methods particularly neural network (NN) in IWP retrieval from passive radiometers. By collocating the MWHS aboard NOAA-18 with Cloud Profiling Radar (CPR) aboard CloudSat, Holl et al. [13] trained an artificial NN to retrieve IWP. They further present the Synergistic Passive Atmospheric Retrieval Experiment-ICE (SPARE-ICE) IWP product using combinations of the MHS MW observations and the Advanced Very High Resolution Radiometer (AVHRR) infrared (IR) observations [14]. Islam and Srivastava [15] also present a work making use of combinations of AMSU-A (MW), MHS (MW), and HIRS (IR) observations to directly retrieve IWP and liquid water path (LWP). A simulation study was carried out by Mastro et al. [16] to evaluate the IWP retrieval performance using observations from the Infrared Atmospheric Sounding Interferometer-New Generation (IASI-NG) and the Microwave Sounder (MWS) aboard the Metop-SG A satellite of the EPS-SG program which will be launched at the beginning of 2025. They found the retrieval performance was advantageous compared with that using IR or MW data only. Amell et al. [17] used a convolutional NN (CNN) to obtain a good IWP retrieval performance with only IR measurements from the geostationary satellite Meteosat-9. Werner et al. [18] introduced an improved cloud detection algorithm for the Aura Microwave Limb Sounder (MLS) based on a feedforward artificial neural network and gained an enhanced classification performance compared with the current version of the "Level 2" MLS cloudiness flag. Liu et al. [19] proposed an inversion method for the remote sensing of ice clouds at terahertz wavelengths based on a genetic algorithm. Larosa et al. [20] described a cloud detection algorithm based on an NN for the MWSs aboard EPS and MetOp-SG. Dong et al. [21] presented a retrieval methodology based on the Bayesian NN (BNN) that inverts the IWP, mean mass-weighted diameter, and cloud height of ice clouds from submillimeter radiometer observations.

Collocating the high-accuracy active cloud radar and the wide-coverage passive radiometer, more global ice cloud information can be obtained using the existing satellite historical observations. The IWP retrieval from FY-3B MWHS based on deep NNs (DNNs) has been presented in [22]. The results show good agreement in the global year map and zonal mean with CloudSat and CALIPSO Ice Cloud Characterization product (2C-ICE). However, there is still room for improvement, especially in the Tibetan Plateau region in winter, where the retrieval results show significantly high outliers. We discussed this to be related to the specific environment of high altitude and need more surface temperature and air temperature information. In this study, observations from the 89- and 118-GHz channels of FY-3D MWHS-II were additionally used. On the training data, we replaced the scanning angle in the previous paper with observation zenith and azimuth angles as the auxiliary parameters to reconstruct the observation geometry for the deep learning models. On the retrieval model, although NN is a general model, its performance is significantly affected by the model hyperparameters, which need to be adjusted iteratively. In this IWP retrieval framework, we adopt a tree-based model and Bayesian-based NN model for the two different tasks of binary classification and regression (corresponding to the two objectives of ice cloud detection and IWP retrieval). Both the models selected here are easy to use and insensitive to hyperparameter tuning. The deep learning framework which combines deep forest (DF21) [23] and quantile regression NNs (QRNNs) [24] is adopted for IWP retrieval from MW brightness temperatures (BTs). The DF21 has been used in near-surface air pollutants' estimation from satellite remote sensing [25], [26] and the QRNN is the core of the NN-based Goddard Profiling Algorithm (GPROF-NN) which has been designed as a drop-in replacement for GPROF used in the operational global precipitation measurement (GPM) processing pipeline [27]. The objective of this article is to further develop and validate the deep learning method in retrieving IWP from the current MWHS-II sounder on-board the FY-3 C/D/E series (from 2013 onward).

This article is structured as follows. In Section II, we provide an overview of the reference IWP product, observations from MWHS-II, and the collocation method. In Section III, we describe the retrieval framework and implementation of deep learning models. The performance of deep learning models is analyzed and discussed in Section IV, including a tropical cyclone case study and a comparison of global means. In Section V, we present conclusions.

II. Dataset

The deep learning algorithms make use of the collocation data from radar and radiometer products which serve as the training database. This section provides an overview of the retrieval database and the collocation strategy.

A. IWP Product

The 2C-ICE is the Level-2C official product of CloudSat to provide cloud properties (IWP, ice water content, mean mass height, mean mass size) with the horizontal and vertical resolutions of 1.4 km and 240 m, respectively. Using the combined inputs from the CPR on CloudSat and the Cloud-Aerosol Lidar with Orthogonal Polarization (CALIOP) on Cloud-Aerosol Lidar and Infrared Pathfinder Satellite Observations (CALIPSO), the retrieval is more tight and can produce more accurate results [28], [29], [30], [31], [32]. However, CloudSat has worked in daylight-only operations mode since April 2011.

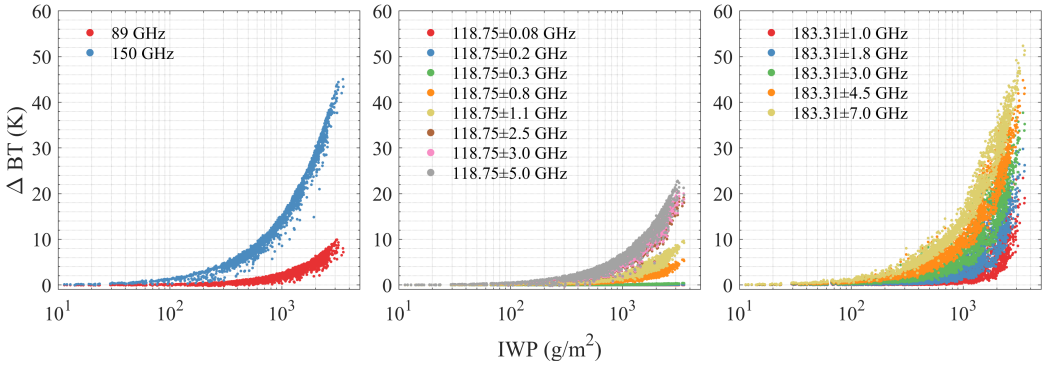

Fig. 1. IWP sensitivity of different channels of MWHS-II.

TABLE I
INSTRUMENT CHARACTERISTICS OF FY-3B/MWHS

Channel	Central Frequency (GHz)	Polarization	Bandwidth (MHz)	NEΔT (K)
1	150	H	1000	0.9
2	150	V	1000	0.9
3	183.31±1.0	H	500	1.1
4	183.31±3.0	H	1000	0.9
5	183.31±7.0	H	2000	0.9

TABLE II
INSTRUMENT CHARACTERISTICS OF FY-3D/MWHS-II

Channel	Central Frequency (GHz)	Polarization	Bandwidth (MHz)	NEΔT (K)
1	89	V	1500	1.0
2	118.75±0.08	H	20	3.6
3	118.75±0.2	H	100	2.0
4	118.75±0.3	H	165	1.6
5	118.75±0.8	H	200	1.6
6	118.75±1.1	H	200	1.6
7	118.75±2.5	H	200	1.6
8	118.75±3.0	H	1000	1.0
9	118.75±5.0	H	2000	1.0
10	150	V	1500	1.0
11	183.31±1.0	H	500	1.0
12	183.31±1.8	H	700	1.0
13	183.31±3.0	H	1000	1.0
14	183.31±4.5	H	2000	1.0
15	183.31±7.0	H	2000	1.0

The combination of CPR and CALIOP provides a more complete and accurate measurement of ice clouds than any other current spaceborne measurements. Further study showed that this combined retrieval method is less sensitive to the changes in the assumed microphysical properties than CPR or CALIOP single retrieval and leads to better agreement with in situ data [33], [34]. The dataset used in this study (version P1_R05) can be obtained from CloudSat DPC [32].

B. Passive Microwave Measurement

The MWHS on FY-3B satellite launched in November 5, 2011 and its successor MWHS-II on FY-3D satellite launched in November 15, 2017 is the main payload for atmospheric water vapor measurement. The MWHS-II on FY-3C was not considered since its equatorial crossing time (ECT) is in the morning. The instrumental parameters are listed in Tables I and II [35], [36]. MWHS contains two 150 GHz with different polarizations and three channels around the 183.31-GHz water vapor line. Compared with MWHS, MWHS-II uses an 89-GHz channel in the atmospheric transparent window instead of the horizontal polarization channel at 150 GHz and also includes eight oxygen sounding channels at 118.75 GHz. In addition, MWHS-II has two more additional channels at 183.3 to complement the three channels of MWHS. As shown in previous studies, the main effect of ice clouds on the MW band is scattering which will lower the observed BT. It is the most pronounced effect in the window channels and the far-wing channels, which means that MWHS-II will have more information about ice clouds than MWHS. The Level-1B BT products of FY-3B/MWHS and FY-3D/MWHS-II are used in this study.

The sensitivity of MWHS-II to different IWP is shown in Fig. 1. The ΔBTs are the brightness temperature difference between simulations in the clear-sky and cloudy conditions at a nadir observation view versus IWPs for different channels calculated by the Atmospheric Radiative Transfer Simulator

(ARTS) with 5000 cloud profiles from the European Centre for Medium-Range Weather Forecasts (ECMWF) 91-level short-range forecasts [37], [38]. The 89-GHz window channel demonstrates sensitivity only when the IWP is above 10^3 g/m^2 due to its large transmittance. The BT sensitivity of the 150-GHz window channel is notable even when the IWP is below 10^3 g/m^2, the largest ΔBT difference could be up to 45 K under our reference cloud scenes. The 118-GHz channels with an offset of $\geq$0.8 GHz show similar sensitivity to the 89-GHz channel, while the 118-GHz channels with an offset of $\geq$2.5 GHz have the larger ΔBT. This is not surprising since the 118-GHz channels are primarily used to measure temperature profiles and the channels with an offset of $\leq$0.8 GHz are sensitive to O_2 from 100 to 30 hPa which is usually higher than where the ice clouds exist. For the 183-GHz channels which are designed for sensing water vapor profiles, all the channels have the sensitivity and the biggest ΔBT is up to 50 K. Thus, the 150- and 183-GHz channels are the main channels that make the radiometer capable of sensing ice clouds as used in the previous research. However, the 89- and 118-GHz channels are also expected to play a role in retrieval since they are sensitive to different atmospheric background variables (surface and temperature profile) beyond ice clouds. In addition, all the channels show little sensitivity when the IWP is below 10^2 g/m^2, and it is therefore selected as the clear-sky IWP threshold in this study.

C. Collocation

The collocation method has been described in the previous study [22]. A time window of 15 min and a spatial distance filter of 7.5 km are applied in collocation since the ECT of FY-3D and CloudSat/CALIPSO is 14:00 and 13:45 asc, respectively, and the space resolution of MWHS-II is 15 km at 150/183 GHz and 30 km at 89/118 GHz. It is a compromise between closer collocating atmospheric scenes and obtaining enough collocations. According to this collocation strategy, multiple 2C-ICE pixels will be included in one MWHS-II pixel and the 2C-ICE pixels will be averaged to obtain the representative value for each collocation. Being MWHS-II a cross-track scanner, IWP is retrieved from different observation view angles and CloudSat IWP is vertically integrated, and such a collocation will undoubtedly introduce additional errors from mixed pixels and radiative transfer paths. It is difficult to avoid. Therefore, we choose scenes with a uniform distribution of IWPs as much as possible. Since the collocated radar pixels can only cover 15% of the area of one MWHS-II pixel (i.e., $\leq$15 pixels), the minimum number of radar pixels ($\geq$10 pixels) and the coefficient of variation ($\leq$0.6) which describe the ice cloud homogeneity were used to further filter the data.

Since 2C-ICE is only available during A-Train or C-Train epochs and CloudSat has suffered reaction wheel anomaly in 2018, 2C-ICE products from January 2018 to September 2018 and after July 10, 2019 are currently vacant (data from July 11, 2019 to August 26, 2020 will be released in the future). Therefore, collocations can only be obtained for almost 12 months. MWHS-II observations from November 2017 to July 2019 were used in the collocation. Finally, in total about 5×10^6 pixels of MWHS-II with reference IWP data were randomly split into a training dataset, validation dataset, and testing dataset of 70%, 15%, and 15%, respectively. Due to the requirements of further analysis, an independent monthly dataset (about 8×10^5 collocated pixels in December 2018, not in the datasets above) was extracted. Based on the IWP threshold for MWHS-II discussed above, about 18% samples have flagged with ice clouds. In addition, the collocations of FY-3B/MWHS and 2C-ICE in 2013 and 2014 were also retrained using the same training strategy for further comparison.

III. Methodology

A. Retrieval Framework

Fig. 2 shows the overall framework of IWP retrieval. First, the 2C-ICE data and MWHS-II observations are preprocessed to control the data quality and collocated to build the retrieval database. Then the collocated observations and the corresponding auxiliary parameters derived from L1B data consisting of observation geometry (zenith, azimuth), geolocation (longitude, latitude), landcover, land–sea mask, and DEM served as retrieval inputs. The deep learning retrieval framework includes two parallel parts, i.e., IWP retrieval and ice cloud detection. IWP retrieval is a regression problem that is solved by the QRNN model. The output of the QRNN model is the values for different quantiles and the mean value is used in our study. For ice cloud detection, DF21 is implemented as the classifier. The outputs of the two parts are filtered to produce the final results. The output of the DF21 model for classification is the binary values (i.e., 0 for false and 1 for true) used as the ice cloud flag. These two models were trained independently, where the QRNN model was trained using only data with an IWP $\geq 10^2$ g/m^2, while the DF21 model used all the training data, with $>10^2$ g/m^2 being 1 and $\leq 10^2$ g/m^2 being 0. For final filtering, we used the false values (i.e., 0) from the DF21 model output to replace the corresponding positions of the QRNN output to produce the final results. This is done to ensure that IWP retrieval is not affected by ice cloud misidentification and to facilitate classification model training since the tree-based algorithms are insensitive to feature scaling.

B. Deep Learning Models

1) QRNN for IWP Retrieval: The regression model QRNN is a flexible nonlinear approach for fitting statistical relationships to quantile functions of conditional probability distributions and is used to estimate the posterior distribution of Bayesian retrievals; it has been applied to remote sensing of variables with mixed discrete-continuous distributions [24], [39]. For remote sensing of atmospheric variables such as precipitation, cloud water path, or IWP that mainly rely on the Bayesian method, the traditional regression NNs using mean squared error (mse) as loss function cannot provide the probabilistic output, while the QRNN can model aleatoric uncertainty and produce a robust regression performance [17].

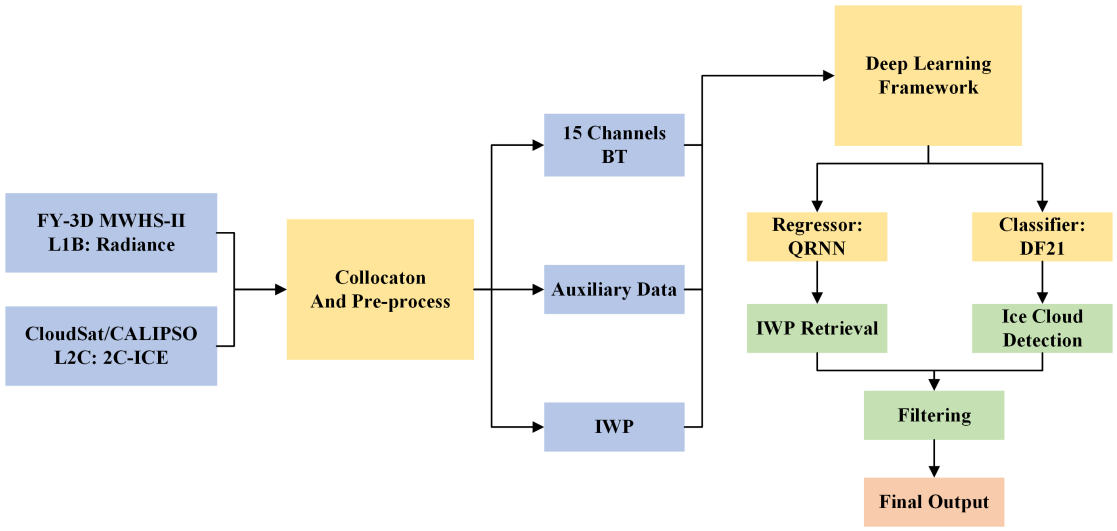

Fig. 2. Overall retrieval framework, including data collocation, training dataset preparation, and structure of deep learning.

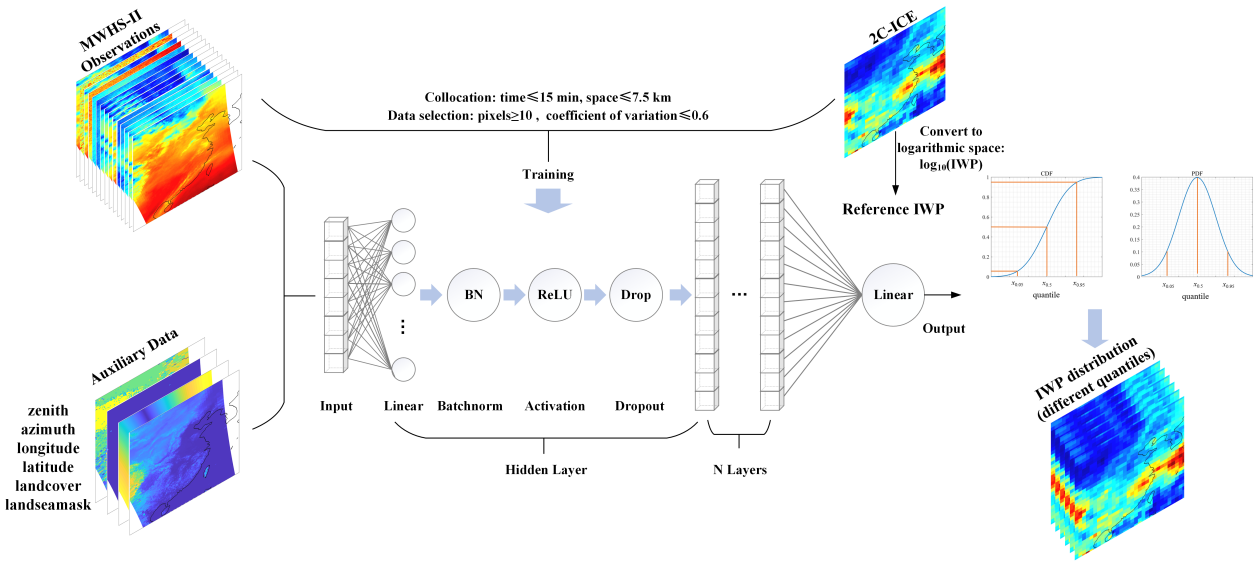

Fig. 3. NN architecture used in IWP regression. The network consists of several hidden layers. Each hidden layer consists of a fully connected layer, batchnorm layer, ReLU activation function, and dropout layer.

The expectation with respect to x of the quantile loss function [40] is defined as follows:

$$\mathcal{L}_\tau(x_\tau, x) = \begin{cases} \tau|x - x_\tau|, & x_\tau \le x \\ (1-\tau)|x - x_\tau|, & \text{otherwise} \end{cases} \quad (1)$$

$$x_\tau = \inf\{x : F(x) \ge \tau\} \quad (2)$$

$$\mathcal{L}(x) = \frac{1}{N}\sum_{i=0}^{N} \mathcal{L}_{\tau_i}(\hat{x}_i, x) \quad (3)$$

where x is the target variable, x_τ is the τth quantile, $F(x)$ is the cumulative distribution function, and $\hat{x}_i$ is the predicted quantile.

QRNN is a universal method that enables different NN architectures. Here it is based on a multilayer perceptron (MLP) which is illustrated in Fig. 3. The MLP has several hidden blocks consisting of a fully connected layer followed by batch normalization (BN) [41] and rectified linear units (ReLU) [42] activation functions. Dropout was also used to prevent model overfitting and improve generalization [43]. The numbers of hidden blocks and neurons in each hidden layer have been experimented and only a little impact on the retrieval performance was found. Finally, we selected a configuration with six hidden layers and 128 neurons. The training is performed over 150 epochs using the Adam optimizer [44] with a base learning rate of 5×10^{-4} a cosine-annealing learning rate schedule. In the training, IWP is transferred to logarithmic space with a base of 10.

2) DF21 for Ice Cloud Detection: In the part of ice cloud detection, the deep forest model DF21 is adopted as the cloud classifier. It is a cascade of random forests which contain numerous decision trees in each forest. DF21 uses the gcForest (multigrained cascade forest) approach to construct a non-NN-style deep model. The model enables representation learning by forest and it uses multigrained scanning which

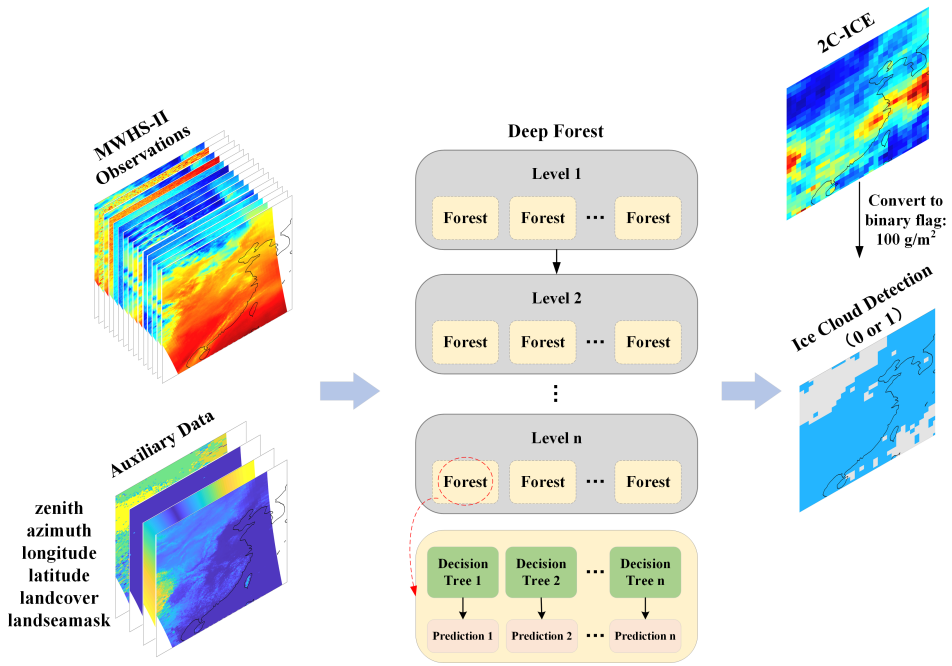

Fig. 4. Deep forest architecture used in ice cloud detection. The deep forest consists of several forests and each forest consists of several trees.

is like the "convolution kernel" in CNNs to enhance its representational learning ability. The cascade levels in DF21 are automatically determined which enables gcForest to work well with small-scale data. Another advantage of DF21 is the fewer hyperparameters than the DNN, and its performance is quite robust to hyperparameter settings.

The DF21 architecture is shown in Fig. 4. The cascade forests include several layers of parallel forests, and the individual forest can use a certain ensemble algorithm (e.g., random forest [45], XGBoost [46], and Lightgbm [47]). In this study, XGBoost is selected as the predictor. The number of deep layers is adaptively regulated by comparing the k-Folder cross-validation accuracy of the current layer with the previous one and the early stopping will be performed if there is no accuracy improvement. In normal random forest models, the final prediction is performed by aggregating predictions of decision trees assigned with the same weight. The prediction of the deep forest model is achieved by aggregating predictions of random forests which combines the advantages of decision tree models and DNNs.

C. Evaluation Metrics

To evaluate the retrieval results, we used several statistical metrics to assess model performance by comparing the predicted variable with the corresponding true measurements in the test dataset.

For IWP retrieval, the used evaluation metrics for regression problems include root mean square error (RMSE), mean absolute percentage error (MAPE), mean bias error (MBE), determination coefficient (R^2), and Pearson correlation coefficients (PCCs). R^2 and PCC reflect the model fitting capability

$$\mathrm{RMSE} = \sqrt{\frac{1}{N}\sum_{i=1}^{N}(y_{\mathrm{pred},i} - y_{\mathrm{true},i})^2} \tag{4}$$

$$\mathrm{MAPE} = \frac{1}{N}\sum_{i=1}^{N}\frac{|y_{\mathrm{pred},i} - y_{\mathrm{true},i}|}{y_{\mathrm{true},i}} \times 100\% \tag{5}$$

$$\mathrm{MBE} = \frac{1}{N}\sum_{i=1}^{N}(y_{\mathrm{pred},i} - y_{\mathrm{true},i}) \tag{6}$$

$$R^2 = 1 - \frac{\sum_{i=1}^{N}(y_{\mathrm{pred},i} - y_{\mathrm{true},i})^2}{\sum_{i=1}^{N}(y_{\mathrm{pred},i} - \overline{y_{\mathrm{true}}})^2} \tag{7}$$

$$\mathrm{PCC} = \frac{\frac{1}{N}\sum_{i=1}^{N}(y_{\mathrm{pred},i} - \overline{y_{\mathrm{pred}}})\sum_{i=1}^{N}(y_{\mathrm{true},i} - \overline{y_{\mathrm{true}}})}{\sigma_{\mathrm{pred}}\sigma_{\mathrm{true}}}. \tag{8}$$

The performance scores used for cloud detection used binary classification metrics based on a confusion matrix for the two cases (i.e., clear-sky and cloudy) which is defined as

$$M = \begin{bmatrix} \mathrm{TP} & \mathrm{FP} \\ \mathrm{FN} & \mathrm{TN} \end{bmatrix}. \tag{9}$$

TP and TN are the number of true positives and true negatives, respectively. FP and FN are the number of false positives and false negatives, respectively.

The used evaluation metrics include accuracy (Acc), false alarm ratio (FAR), precision, recall (also called probability of detection, POD), F1 score, and critical success index (CSI). The accuracy describes the percentage of accurate model predictions, but since the ice cloud samples are a relatively small percentage of the total data, this metric does not reflect the detection capability of the model well. Therefore, the following indicators are needed. The FAR describes the proportion of model error detection of ice clouds. Precision is the fraction of correctly detected ice cloud pixels of all the pixels predicted to be with ice clouds, and recall is the fraction of all the true ice cloud pixels that are correctly detected. The pursuit of low FAR alone will result in lower POD and failure to detect ice clouds, and vice versa. Therefore, several indicators need to be considered together. F1 assigns more relevance to

TABLE III
DIFFERENT INPUT COMBINATIONS USED IN THE TRAINING

Name	Channels	Auxiliaries
MWHS-II$_4$	10, 11, 13, 15	/
MWHS-II$_5$	1, 10, 11, 13, 15	/
MWHS-II$_7$	1, 10-15	/
MWHS-II$_{12}$	1, 5-15	/
MWHS-II$_{15}$	1-15	/
MWHS$_{5,aux}$(1-year)	1-5	zenith, azimuth, longitude, latitude, landcover, landseamask
MWHS$_{5,aux}$(2-years)	1-5	zenith, azimuth, longitude, latitude, landcover, landseamask
MWHS-II$_{15,aux}$	1-15	zenith, azimuth, longitude, latitude, landcover, landseamask, DEM

false predictions and is more suitable for imbalanced classes, where the respective data sizes vary significantly. CSI which combines FAR and POD is a more comprehensive indicator that is commonly used in precipitation retrieval [48]. Combining these metrics can better evaluate the classification results when the positive and negative samples are not homogeneous

$$\text{ACC} = \frac{\text{TP} + \text{TN}}{\text{TP} + \text{TN} + \text{FN} + \text{FP}} \tag{10}$$

$$\text{FAR} = \frac{\text{FP}}{\text{TP} + \text{FP}} \tag{11}$$

$$\text{Precision} = \frac{\text{TP}}{\text{TP} + \text{FP}} \tag{12}$$

$$\text{Recall} = \frac{\text{TP}}{\text{TP} + \text{FN}} \tag{13}$$

$$F1 = \frac{2 \times (\text{Precision} \times \text{Recall})}{\text{Precision} + \text{Recall}} \tag{14}$$

$$\text{CSI} = \frac{\text{TP}}{\text{TP} + \text{FN} + \text{FP}}. \tag{15}$$

IV. RESULTS

This section presents the results of ice cloud retrieval using the deep learning framework. Sections IV-A and IV-B evaluate the performance of IWP retrieval and ice cloud detection using a separate test dataset. Section IV-C evaluates the complete retrievals combining the two models. The remainder of this section presents a case study of IWP retrievals from a tropical cyclone and is followed by an analysis of global/zonal monthly mean results.

A. IWP Retrieval Performance

In the previous study [22], the IWP retrieval performance of different channels and auxiliaries of FY-3B/MWHS was analyzed. The 150- and 183-GHz channels of MWHS show a good performance in IWP retrieval using DNNs. Here, we further compare the performance of QRNN with DNN and evaluate the impacts of new channels in FY-3D/MWHS-II. The different input combinations in the training evaluation are defined in Table III. For channel selection, MWHS-II$_4$ represents the same channel as MWHS and MWHS-II$_5$ will represent the impact of the 89-GHz channel. MWHS-II$_7$ is used to evaluate the improvement of the new 183-GHz channels and MWHS-II$_{12}$ shows the impact of the 118-GHz channels which have obvious responses to ice cloud. MWHS-II$_{15}$ indicates that IWPs are estimated from all the channels. The subscript "aux" represents the addition of observation auxiliary information, which has been proven to be effective in previous studies.

The corresponding evaluation metrics are shown in Table IV. It was shown that the inclusion of the 89-GHz channel (MWHS-II$_5$ with respect to MWHS-II$_4$) provides a significant improvement with RMSE and MBE decreased from 920.953 to 811.941 g/m^2 and -100.93 to -69.491 g/m^2, respectively. MAPE decreased from 94.138% to 78.545%. R^2 increased from 0.484 to 0.591, and PCC increased from 0.702 to 0.778. Although the 89-GHz channel is not very sensitive to the changes in IWP, it provides information about the surface background of the observation. It is very helpful since the MW radiometer obtains ice cloud information by observing changes in BT which will also be affected by the surface. The 118-GHz channels with offset larger than 0.8 GHz (i.e., MWHS-II$_{12}$) also show large performance enhancement with RMSE, and MBE decreased to 737.558 and -60.856 g/m^2, MAPE decreased to 59.896%, R^2 increased to 0.669, and PCC increased to 0.822. However, the contribution of two new 183-GHz channels (i.e., MWHS-II$_7$) and the first three 118-GHz channels (i.e., MWHS-II$_{15}$) is relatively small. This is expected since the 118-GHz channels are near the peak to the oxygen line, and the two additional channels at 183.3 GHz provide information on ice particles that is much correlated to the information from the other channels.

The addition of auxiliaries has a significant improvement on the MWHS model, while the improvement on the MWHS-II model is minimal. This indicates that the information content in MWHS channels is far from enough and needs to be supplemented by auxiliaries, while MWHS-II has enough channel information content. Nevertheless, adding inputs does not have a negative effect, and thus, the final model uses all the inputs. It should be mentioned that we found no additional improvement when adding scan angles in the previous study and then we believe that the zenith and azimuth angles are all needed to construct the complete geometry, which is evidenced in this study. Comparing the results of the QRNN model and the DNN model, QRNN is better in most metrics. As discussed in the previous study, MAPE and MBE are contradictory metrics. DNN using mse loss function will produce a larger bias but the relative error will be smaller, while QRNN uses quantile loss to balance MAPE and MBE, making the overall model superior. Both MWHS and MWHS-II demonstrate similar findings. In addition, for MWHS retrieval, one and two years of collocated datasets were used for model training, respectively, marked as MWHS$_{5,\text{aux}}$ (one-years) and

TABLE IV
EVALUATION METRICS IN IWP RETRIEVAL USING DIFFERENT CHANNELS AND AUXILIARIES

Inputs	RMSE (g/m^2)	MAPE (%)	MBE (g/m^2)	R^2	PCC
MWHS-II$_4$, QRNN	920.953	94.138	-100.930	0.484	0.702
MWHS-II$_5$, QRNN	811.941	78.545	-69.491	0.591	0.778
MWHS-II$_7$, QRNN	807.449	73.928	-72.249	0.604	0.782
MWHS-II$_{12}$, QRNN	737.558	59.896	-60.856	0.669	0.822
MWHS-II$_{15}$, QRNN	736.102	56.881	-73.230	0.670	0.825
MWHS$_{5,aux}$(1-years), QRNN	876.788	77.856	-82.017	0.561	0.759
MWHS$_{5,aux}$(1-years), DNN	916.410	65.131	-156.300	0.521	0.732
MWHS$_{5,aux}$(2-years), QRNN	851.670	78.978	-78.310	0.573	0.764
MWHS$_{5,aux}$(2-years), DNN	869.556	64.836	-124.069	0.555	0.752
MWHS-II$_{15,aux}$, QRNN	730.142	54.385	-73.683	0.676	0.827
MWHS-II$_{15,aux}$, DNN	800.677	50.869	-100.604	0.610	0.785

TABLE V
EVALUATION METRICS IN ICE CLOUD DETECTION USING DIFFERENT CHANNELS AND AUXILIARIES

Inputs	ACC	FAR	Precision	Recall	F1	CSI
MWHS-II$_4$, DF21	0.908	0.269	0.731	0.602	0.660	0.492
MWHS-II$_5$, DF21	0.915	0.230	0.770	0.611	0.681	0.517
MWHS-II$_7$, DF21	0.918	0.224	0.776	0.631	0.697	0.535
MWHS-II$_{12}$, DF21	0.932	0.174	0.826	0.685	0.749	0.599
MWHS-II$_{15}$, DF21	0.936	0.164	0.836	0.708	0.766	0.621
MWHS$_{5,aux}$(1-year), DF21	0.935	0.179	0.821	0.727	0.771	0.627
MWHS$_{5,aux}$(1-year), DNN	0.923	0.205	0.795	0.666	0.725	0.568
MWHS$_{5,aux}$(2-years), DF21	0.935	0.183	0.817	0.724	0.767	0.623
MWHS$_{5,aux}$(2-years), DNN	0.923	0.219	0.781	0.665	0.719	0.561
MWHS-II$_{15,aux}$, DF21	0.946	0.148	0.852	0.773	0.810	0.681
MWHS-II$_{15,aux}$, DNN	0.936	0.162	0.838	0.709	0.768	0.624

MWHS$_{5,\text{aux}}$ (two-years). However, there is no difference in the results, indicating that one year of collocation data is sufficient for the model to learn the features of the data.

B. Cloud Detection Performance

Ice cloud detection is a binary classification problem, and the DF21 model and the DNN model with sigmoid function are compared in this section. Concerning the detection metrics shown in Table V, the performances for different input combinations are mostly consistent with the results of IWP retrieval shown above. However, there still exist some differences. The 89-GHz channel mainly decreases FAR from 0.269 to 0.230 but increases recall little, from 0.602 to 0.611. The new 183-GHz channels perform the opposite to decrease FAR from 0.230 to 0.224 and increase recall from 0.611 to 0.631. Both the F1 score and CSI are improved. ACC and precision are also enhanced. The 118-GHz channels give a large improvement in cloud detection, especially the important metrics FAR and recall are decreased to 0.164 and increased to 0.708, respectively. F1 score and CSI are increased to 0.766 and 0.621, respectively. Compared with IWP retrieval, the first three channels of 118 GHz are more effective in ice cloud detection, probably because the formation of ice clouds is closely related to the atmospheric temperature.

The auxiliary information also show a great contribution to cloud detection since the collocation method has certain limits. CPR is a nadir observation sensor, while MWHS/MWHS-II is a cross-track scanning sounder, which leads to the problem of inconsistent observation paths in the collocation. The inputs of observation geometry can alleviate this problem to some extent. In addition, MWHS/MWHS-II uses the observed ΔBT due to ice particle scattering to detect ice clouds, which will also be affected by the local atmospheric temperature, for example, in the Tibetan plateau or polar regions. Therefore, observational geographic information can contribute. For MWHS retrieval, the auxiliary information reduces the FAR to 0.179 and increases precision, recall, F1, and CSI to 0.821, 0.727, 0.771, and 0.627, respectively. In contrast, MHWS-II has more channels for the detection of ice clouds, so the role of auxiliary information becomes small in the results. Comparing the results of the DF21 model and DNN model, DF21 is superior to DNN in all the metrics and has good robustness of model training, while DNN is more sensitive to hyperparameters. As with IWP retrieval, the MHWS retrieval result for the two-year training dataset does not exhibit higher performance than MWHS for the one-year training dataset.

C. Final Test Results

The final selected models are MWHS-II$_{15,\text{aux}}$ input combination based on QRNN and DF21. The test results are shown in Table VI with different surface types. For all the surfaces, MAPE and MBE are increasing a little from 54.385% to 65.122% and -73.683 to -104.232 g/m^2 due to misdetection of ice clouds and the other metrics are similar. For different surface types, the metrics of ocean surface are significantly better than that of land. This is because the ocean surface and the atmospheric environment are more stable as a background for observation than land, making it easier to detect and measure ice clouds. Forests and snow and ice are the regions with poor retrieval accuracy. RMSE and MBE of forest surface

TABLE VI
EVALUATION METRICS IN THE COMPLETE RETRIEVAL FOR ALL IWP ≥ 100 g/m^2 IN 2C-ICE

Surface type (numbers)	RMSE (g/m^2)	MAPE (%)	MBE (g/m^2)	R^2	PCC
All surface (17258)	707.346	65.122	-104.232	0.683	0.831
Land (4729)	796.740	65.598	-141.074	0.648	0.813
Ocean (11673)	678.277	64.647	-90.982	0.697	0.838
Forests (1093)	1138.430	67.022	-209.593	0.602	0.787
Shrub lands (1189)	506.193	61.406	-119.908	0.708	0.852
Snow and Ice (1160)	226.986	63.625	-95.675	0.488	0.765

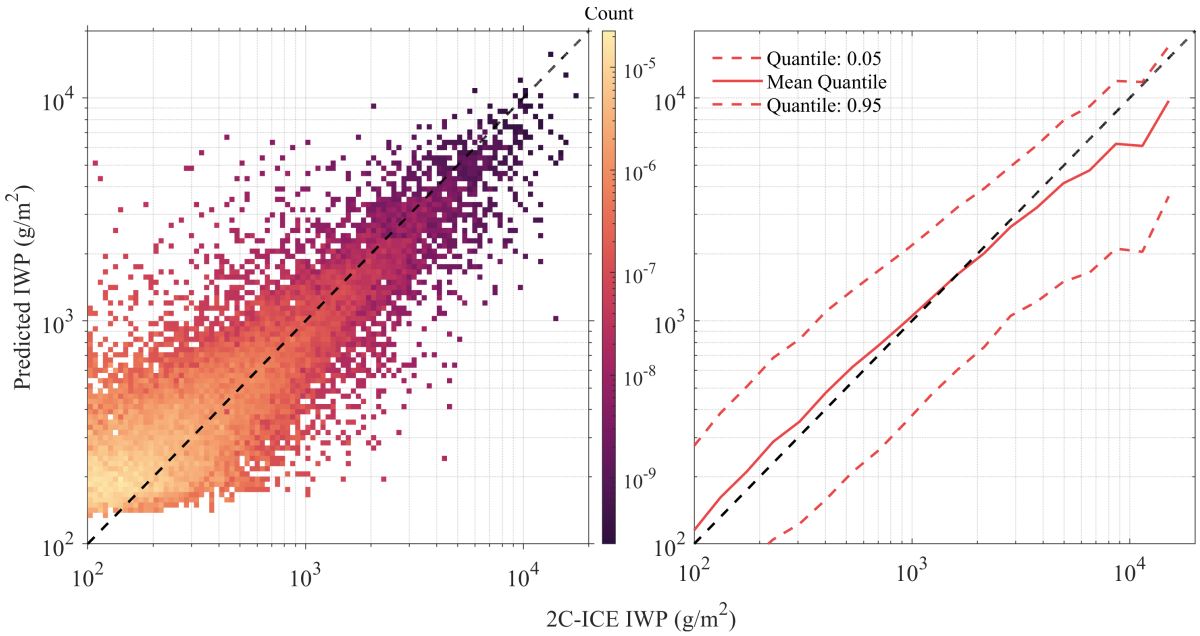

Fig. 5. Comparison between 2C-ICE and deep learning retrieved IWP from MWHS-II observations.

increase to 1138.430 and −209.593 g/m^2, respectively. Most of the evaluation metrics for snow and ice surface are considered satisfactory, except for a low R^2, which is likely due to the small sample size and the lower IWP in the polar region. Fig. 5 shows the scatter comparison between 2C-ICE and MWHS-II IWP, and the mean IWPs for different quantiles in the retrieval. The result shows relative agreement, and the mean IWPs' line is closer to the identity line. However, it still overestimates the IWPs around 10^2 g/m^2 due to the lack of sensitivity of the MW channels to thin ice clouds. It also underestimates the IWPs around 10^4 g/m^2, and this may be because there are fewer IWP cases of this magnitude in the collocation database leading to insufficient training. The 0.05 and 0.95 quantile mean IWPs' lines show the extremal quantile levels which indicate the predicted value limits.

D. Case Study: Tropical Cyclone

The results described above were based on the test dataset extracted from the collocation database and have the same statistics. Therefore, it is necessary to validate and analyze other representative cases. Tropical cyclone CILIDA in the Southern Indian Ocean on December 24, 2018, observed by FY3B/MWHS, FY3D/MWHS-II, and CloudSat with a little time delay (the time difference of MWHS-II and 2C-ICE is approximately 19 min; the time difference of MWHS and 2C-ICE is approximately 105 min), was selected for this testing target. Fig. 6 shows the retrieval results and collocation comparison with 2C-ICE from MWHS, MWHS-II, and ERA5. The ERA5 IWPs were combined from the total column snow water (CSW) and cloud ice water (CIW). It should be noted that although in the ECMWF model convective rain and snowfall exist as prognostic variables, these two classes are not part of ERA5's set of variables. The comparison with ERA5 is limited in case of the presence of convection. The retrieved IWPs from MWHS/MWHS-II in the cyclone region are similar to a distinct cyclonic structure, while IWPs from ERA5 are only a vague shape. Since 2C-ICE has only a very narrow spacial coverage, the results cannot be compared in terms of cyclone structure. Thus, a collocation was done between MWHS, MWHS-II, ERA5, and 2C-ICE to evaluate the results. From the scatter plot, both MWHS and MWHS-II retrievals are closer to the identity line while ERA5 significantly underestimates the IWPs when they are larger than 10^3 g/m^2. Compared with the MWHS-II results, the MWHS results are more discrete on both sides of the identity line, while the MWHS-II results converge more, but with an inclination angle. However, they both overestimate the true value when IWPs are smaller than 10^3 g/m^2 and underestimate when it is larger. This feature matches the results of the test dataset

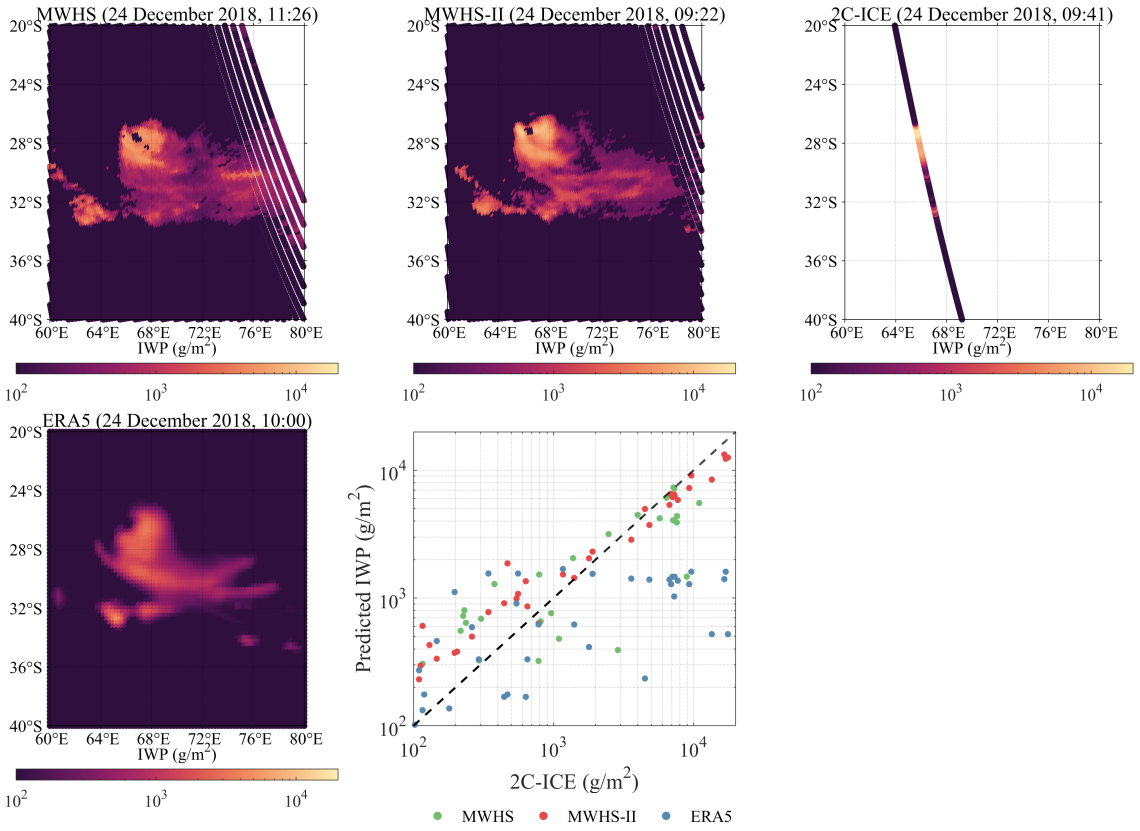

Fig. 6. Comparison of IWPs from MWHS and MWHS-II retrieval, 2C-ICE and ERA5 in a case study of tropical cyclone. UTC time is used.

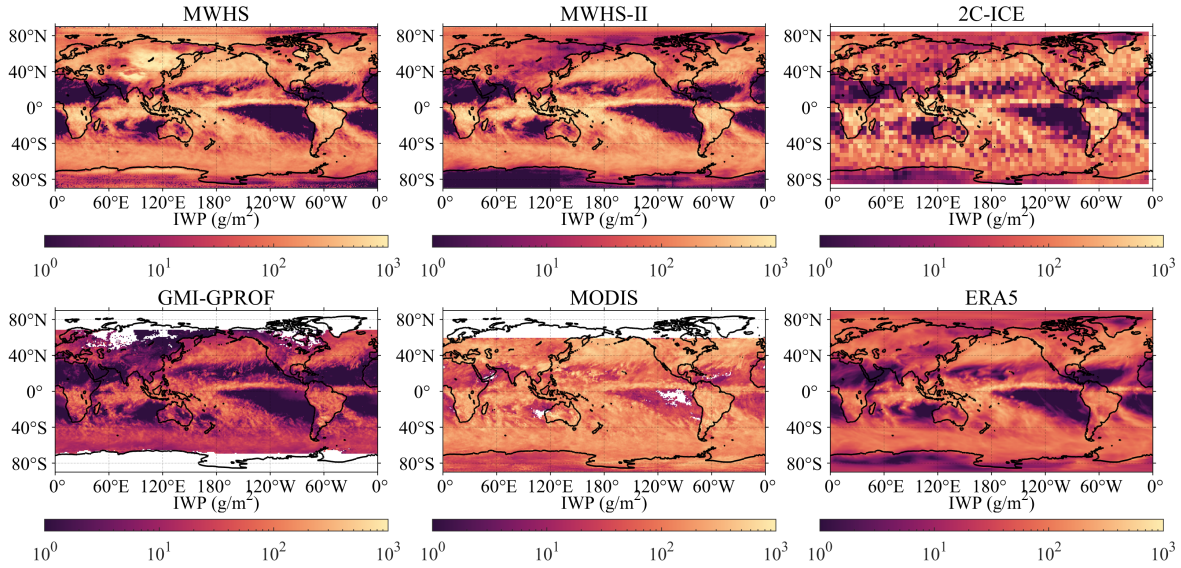

Fig. 7. Global mean IWP maps for December 2018 from MWHS and MWHS-II retrieval, 2C-ICE, GMI-GPROF, MODIS, and ERA5. 2C-ICE is gridded on a 5° grid, while the other products are gridded on a 1° grid.

(see Fig. 5). Table VII shows the specific metrics of cyclone retrievals. MWHS-II shows much better retrieval performance than MWHS, especially R^2 of MWHS-II is 0.901 while that of MWHS is only 0.582.

E. Comparison Results in Global/Zonal Monthly Mean Data

Fig. 7 shows a gridded map for different IWP products for December 2018, and this dataset is independent of the training dataset. MWHS and MWHS-II IWPs were retrieved using the models discussed above. For comparison, GMI Level 3A monthly IWP product (GPM_3GPROFGPMGMI, [49]), MODIS Cloud Properties Level 3 monthly IWP product (MCD06COSP_M3, [50]), and ERA5 reanalysis monthly IWP product [51] were also shown. All the IWPs were sorted into 1° × 1° bins (2C-ICE was into 5° × 5°), and the mean IWP was calculated for each bin.

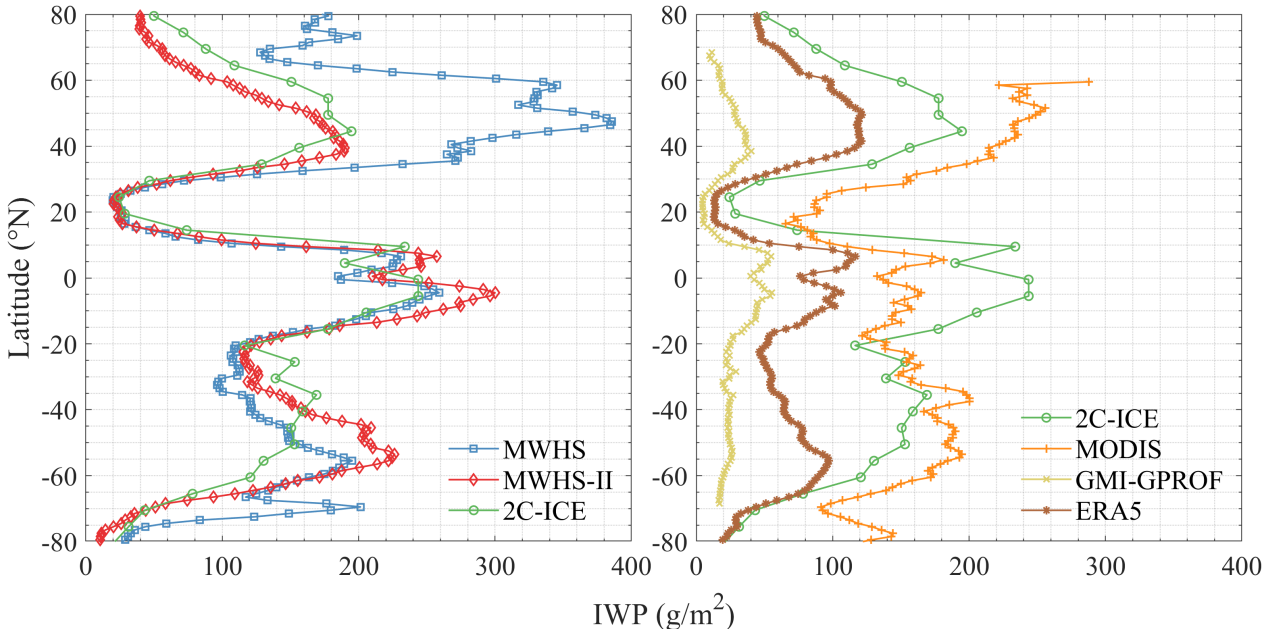

Fig. 8. Zonal means of IWPs for December 2018 from MWHS and MWHS-II retrieval, 2C-ICE, GMI-GPROF, MODIS, and ERA5. 2C-ICE is gridded on a 5° grid, while the other products are gridded on a 1° grid.

TABLE VII
EVALUATION METRICS IN THE CASE OF A TROPICAL CYCLONE

Inputs	RMSE (g/m^2)	MAPE (%)	MBE (g/m^2)	R^2	PCC
$MWHS_{5,aux}$	2130.031	81.872	-839.872	0.582	0.815
$MWHS\text{-}II_{15,aux}$	1598.657	75.987	-555.824	0.901	0.987

All the data share some common IWP characteristics, such as quite high IWP in the intertropical convergence zone, the Pacific warm pool, and quite low IWP in the Sahara and Arabian deserts. Using 2C-ICE IWPs as the reference, there is no doubt that the results from MWHS-II are the closest to the true value and only underestimate IWP in the Antarctic region. The MWHS IWPs show significant overestimation for the northern hemisphere mid and high latitudes, especially in the Siberian region and the Tibetan Plateau. The IWPs of GMI-GPROF are the lowest in these datasets because GMI is mainly used for precipitation observations, and although it contains channels similar to MWHS, the algorithm mainly targets ice particles with significant precipitation conditions. The MODIS IWPs are large in most regions but are small in equatorial convective regions. The IWPs of ERA5 are relatively low overall, but the distribution characteristics are close to 2C-ICE. The zonal means of IWPs shown in Fig. 8 provide a more quantitative comparison of cloud ice estimates from different sensors. MWHS greatly overestimates the IWPs above 30 °N, but is very close to 2C-ICE between 30 °N and 20 °S. The IWPs are also underestimated between 20 °S and 50 °S and overestimated thereafter. Compared with MWHS, MWHS-II IWPs are closer to 2C-ICE, with a clear overestimation of IWPs between 40 °S and 70 °S, and a slight overestimation near the equator. For GMI, MODIS, and ERA5, the overall differences with 2C-ICE are relatively large. The above results show that IWPs based on MWHS-II observations and deep learning models can provide ice cloud information close to 2C-ICE but with greater spatial coverage and time resolution.

V. SUMMARY AND CONCLUSION

This study presents a deep-learning-based implementation of the IWP retrieval algorithm for the MWHS-II instrument aboard FY-3D and other meteorological satellites. The performance of the algorithm is evaluated by comparing it with common satellite products and reanalysis data. By combining the observed BT from MWHS/MWHS-II with the CloudSat product 2C-ICE, and using deep learning models to establish the nonlinear relationship between them, it is possible to obtain IWPs with accuracy that is partially comparable to the radar product. This approach allows for the retention of the wide scanning and high coverage advantages offered by the radiometer. A deep learning framework was used, combining the deep forest model for ice cloud detection and the QRNN model for IWP estimation. Compared with the DNN model, the DF model yields better classification metrics, while the QRNN model provides better constraints on the bias of IWP estimation. The combination of DF21 and QRNN deep learning algorithms demonstrates robustness in retrieving IWP without the need for excessive hyperparameter tuning. By comparing the different model inputs, it is found that the 89-GHz channel and the last five channels of 118 GHz give a significant improvement in the evaluation metrics, which is consistent with the sensitivity analysis. We also found that the influence of the auxiliaries is significant for MWHS channel retrieval, while the influence is relatively small for MWHS-II channel retrieval. In addition, the performance of the model was compared using one and two years of MWHS collocations as training datasets. The results indicate that the model's performance did not improve with two years of training data. This means that even with just one year of training data,

almost full performance can be achieved. This is beneficial for MWHS-II because CloudSat was no longer in conjunction with CALIPSO after August 2020, and the new MWHS-II cannot be collocated with 2C-ICE. The models trained in this study can be applied to MWHS-II on other satellites.

The evaluation of the deep learning algorithm for MWHS/MWHS-II showed that the retrieved IWPs can be more accurately approximated to 2C-ICE. This is particularly true when using the measurements from MWHS-II as inputs, resulting in a mean MAPE of 65%, and R^2 and PCC of 0.68 and 0.83, respectively. The analysis of a tropical cyclone case shows that the near-instantaneous retrieval results of MWHS-II are in strong agreement with 2C-ICE under extreme conditions, with R^2 and PCC both exceeding 0.9. The comparison of monthly IWP products on a larger time scale indicates that the results from MWHS-II provide a reasonable estimate and are most similar to those from 2C-ICE, when compared with MODIS, GMI, and ERA5.

Despite the favorable retrieval performance, there are still limitations that need to be considered. First, it is important to note that there are differences in observation paths and pixel sizes between MWHS/MWHS-II and CPR. These differences cannot be ignored and result in inevitable errors, although we have taken steps to minimize these errors using more than 10 CPR pixels to calculate the mean IWP and filtering using their coefficients of variation. In addition, we have included observation geometry in the training input parameters. To address this issue, we can limit the scan angle of the MWHS/MWHS-II measurements used for collocation. However, this tradeoff step will decrease the number of collocations and restrict them to a specific range, which could potentially hinder global retrieval. MW channels have limited detection capability for thin clouds, resulting in a relatively high FAR compared with IR channels. Although we set the threshold value for the IWP at 100 g/m^2, it is evident that there is a significant deviation from this value. This highlights the need for submillimeter-wave channels in the future. This study demonstrates that deep learning models partially learn to represent 2C-ICE IWPs from MWHS/MWHS-II observations. However, the predicted IWPs do not represent the true atmospheric state. Since the models were trained on the collocated 2C-ICE IWPs, they follow that they, at best, will replicate the respective 2C-ICE results. The results also inherit and amplify the uncertainties and biases of 2C-ICE. Moreover, since CloudSat only works during the daytime, there may be a negative impact on nighttime IWP estimates.

The current observations of MWHS-II are mainly applied to data assimilation without a separate IWP product, but it is also difficult to assimilate the atmospheric scene where ice clouds exist. While the upcoming launch of ICI can improve detection accuracy, it does not address past climate conditions. The use of deep learning methods for retrieving IWP is beneficial. Using over ten years of observations from MWHS-II (FY-3C/D/E), we can provide data support for analyzing the impact of ice clouds on the Earth system from a climatological perspective.

ACKNOWLEDGMENT

The authors thank the deep forest team and Dr. Simon Pfreundschuh for providing the DF21 and QRNN model package (publicly available). They would like to thank the National Satellite Meteorological Center of China Meteorological Administration for providing the archived data of FY-3B MWHS and FY-3D MWHS-II. They also acknowledge the use of data from the CloudSat Data Processing Center which is run by the Cooperative Institute for Research in the Atmosphere (CIRA) at Colorado State University.

REFERENCES

[1] D. E. Waliser et al., "Cloud ice: A climate model challenge with signs and expectations of progress," *J. Geophys. Res., Atmos.*, vol. 114, no. 8, Jan. 2009, Art. no. D00A21.

[2] *Climate Change 2021: The Physical Science Basis. Contribution of Working Group I to the Sixth Assessment Report of the Intergovernmental Panel on Climate Change*, IPCC, Geneva, Switzerland, Jan. 2021.

[3] *The Global Climate Observing System 2021: The GCOS Status Report*, World Meteorological Organization, Geneva, Switzerland, Jan. 2021.

[4] S. A. Buehler et al., "A concept for a satellite mission to measure cloud ice water path, ice particle size, and cloud altitude," *Quart. J. Roy. Meteorological Soc.*, vol. 133, no. 2, pp. 109–128, Nov. 2007.

[5] P. Eriksson et al., "Towards an operational ice cloud imager (ICI) retrieval product," *Atmos. Meas. Techn.*, vol. 13, no. 1, pp. 53–71, Jan. 2020.

[6] S. Pfreundschuh et al., "Synergistic radar and radiometer retrievals of ice hydrometeors," *Atmos. Meas. Techn.*, vol. 13, no. 8, pp. 4219–4245, Aug. 2020.

[7] S. Pfreundschuh et al., "Synergistic radar and sub-millimeter radiometer retrievals of ice hydrometeors in mid-latitude frontal cloud systems," *Atmos. Meas. Techn.*, vol. 15, no. 3, pp. 677–699, Feb. 2022.

[8] Y. Liu and G. G. Mace, "Assessing synergistic radar and radiometer capability in retrieving ice cloud microphysics based on hybrid Bayesian algorithms," *Atmos. Meas. Techn.*, vol. 15, no. 4, pp. 927–944, Feb. 2022.

[9] Y. Liu, G. G. Mace, and D. J. Posselt, "Assessing synergistic radar and radiometer retrievals of ice cloud microphysics for the atmosphere observing system (AOS) architecture," *IEEE Trans. Geosci. Remote Sens.*, vol. 60, 2022, Art. no. 4107714.

[10] W. J. Blackwell et al., "An overview of the TROPICS NASA Earth venture mission," *Quart. J. Roy. Meteorological Soc.*, vol. 144, no. 1, pp. 16–26, Nov. 2018.

[11] C. Kidd, T. Matsui, W. Blackwell, S. Braun, R. Leslie, and Z. Griffith, "Precipitation estimation from the NASA TROPICS mission: Initial retrievals and validation," *Remote Sens.*, vol. 14, no. 13, p. 2992, Jun. 2022.

[12] S. Zhang et al., "Design of the second generation microwave humidity sounder (MWHS-II) for Chinese Meteorological Satellite FY-3," in *Proc. IEEE Int. Geosci. Remote Sens. Symp.*, Munich, Germany, Jul. 2012, pp. 4672–4675.

[13] G. Holl, S. A. Buehler, B. Rydberg, and C. Jiménez, "Collocating satellite-based radar and radiometer measurements—Methodology and usage examples," *Atmos. Meas. Techn.*, vol. 3, no. 3, pp. 693–708, Jun. 2010.

[14] G. Holl, S. Eliasson, J. Mendrok, and S. A. Buehler, "SPARE-ICE: Synergistic ice water path from passive operational sensors," *J. Geophys. Res., Atmos.*, vol. 119, no. 3, pp. 1504–1523, Feb. 2014.

[15] T. Islam and P. K. Srivastava, "Synergistic multi-sensor and multi-frequency retrieval of cloud ice water path constrained by CloudSat collocations," *J. Quant. Spectrosc. Radiat. Transf.*, vol. 161, pp. 21–34, Aug. 2015.

[16] P. Mastro et al., "Combined IASI-NG and MWS observations for the retrieval of cloud liquid and ice water path: A deep learning artificial intelligence approach," *IEEE J. Sel. Topics Appl. Earth Observ. Remote Sens.*, vol. 15, pp. 3313–3322, 2022.

[17] A. Amell, P. Eriksson, and S. Pfreundschuh, "Ice water path retrievals from Meteosat-9 using quantile regression neural networks," *Atmos. Meas. Techn.*, vol. 15, no. 19, pp. 5701–5717, Oct. 2022.

[18] F. Werner, N. J. Livesey, M. J. Schwartz, W. G. Read, M. L. Santee, and G. Wind, "Improved cloud detection for the Aura microwave limb sounder (MLS): Training an artificial neural network on colocated MLS and Aqua MODIS data," *Atmos. Meas. Techn.*, vol. 14, no. 12, pp. 7749–7773, Dec. 2021.

[19] L. Liu, C. Weng, S. Li, L. Husi, S. Hu, and P. Dong, "Passive remote sensing of ice cloud properties at terahertz wavelengths based on genetic algorithm," *Remote Sens.*, vol. 13, no. 4, p. 735, 2021.

[20] S. Larosa et al., "A cloud detection neural network approach for the next generation microwave sounder aboard EPS MetOp-SG A1," *Remote Sens.*, vol. 15, no. 7, p. 1798, Mar. 2023.

[21] P. Dong, L. Liu, S. Li, L. Husi, S. Hu, and L. Bu, "A novel ice cloud retrieval algorithm for submillimeter wave radiometers: Simulations and application to an airborne experiment," *IEEE Trans. Geosci. Remote Sens.*, vol. 61, 2023, Art. no. 2001609.

[22] W. Wang, Z. Wang, Q. He, and L. Zhang, "Retrieval of ice water path from the microwave humidity sounder (MWHS) aboard FengYun-3B (FY-3B) satellite polarimetric measurements based on a deep neural network," *Atmos. Meas. Techn.*, vol. 15, no. 21, pp. 6489–6506, Nov. 2022.

[23] Z.-H. Zhou and J. Feng, "Deep forest," *Nat. Sci. Rev.*, vol. 6, no. 1, pp. 74–86, 2019.

[24] S. Pfreundschuh, P. Eriksson, D. Duncan, B. Rydberg, N. Hakansson, and A. Thoss, "A neural network approach to estimating a posteriori distributions of Bayesian retrieval problems," *Atmos. Meas. Techn.*, vol. 11, no. 8, pp. 4627–4643, Aug. 2018.

[25] S. Zhu et al., "Learning surface ozone from satellite columns (LESO): A regional daily estimation framework for surface ozone monitoring in China," *IEEE Trans. Geosci. Remote Sens.*, vol. 60, 2022, Art. no. 4108711.

[26] S. Zhu et al., "Estimating near-surface concentrations of major air pollutants from space: A universal estimation framework LAPSO," *IEEE Trans. Geosci. Remote Sens.*, vol. 61, 2023, Art. no. 4101011.

[27] S. Pfreundschuh, P. J. Brown, C. D. Kummerow, and P. Eriksson, "GPROF-NN: A neural-network-based implementation of the Goddard profiling algorithm," *Atmos. Meas. Techn.*, vol. 15, no. 17, pp. 5033–5060, Sep. 2022.

[28] G. L. Stephens et al., "CloudSat mission: Performance and early science after the first year of operation," *J. Geophys. Res., Atmos.*, vol. 113, no. 8, Dec. 2008, Art. no. D00A18.

[29] D. M. Winker et al., "Overview of the CALIPSO mission and CALIOP data processing algorithms," *J. Atmos. Ocean. Technol.*, vol. 26, no. 11, pp. 2310–2323, Nov. 2009.

[30] M. Deng, G. G. Mace, Z. Wang, and H. Okamoto, "Tropical composition, cloud and climate coupling experiment validation for cirrus cloud profiling retrieval using CloudSat radar and CALIPSO LiDAR," *J. Geophys. Res., Atmos.*, vol. 115, no. 10, Sep. 2010, Art. no. D00J15.

[31] M. Deng, G. G. Mace, Z. Wang, and E. Berry, "CloudSat 2C-ICE product update with a new Z_e parameterization in LiDAR-only region," *J. Geophys. Res., Atmos.*, vol. 120, no. 23, pp. 12–198, Dec. 2015.

[32] M. Gerald and D. Min, "Level 2 CloudSat-CALIPSO combined ice cloud property retrieval product process description and interface control document," NASA, Washington, DC, USA, Tech. Rep., P1_R05, 2019.

[33] J. Delanoe and R. J. Hogan, "Combined CloudSat-CALIPSO-MODIS retrievals of the properties of ice clouds," *J. Geophys. Res., Atmos.*, vol. 115, no. 4, Jul. 2010, Art. no. D00H29.

[34] M. Deng, G. G. Mace, Z. Wang, and R. P. Lawson, "Evaluation of several A-train ice cloud retrieval products with in situ measurements collected during the SPARTICUS campaign," *J. Appl. Meteorol. Climatol.*, vol. 52, no. 4, pp. 1014–1030, Apr. 2013.

[35] X. Zou, Y. Ma, and Z. Qin, "Fengyun-3B MicroWave humidity sounder (MWHS) data noise characterization and filtering using principle component analysis," *IEEE Trans. Geosci. Remote Sens.*, vol. 50, no. 12, pp. 4892–4902, Dec. 2012.

[36] Z. Wang et al., "Performance analysis of microwave humidity and temperature sounder onboard the FY-3D satellite from prelaunch multiangle calibration data in thermal/vacuum test," *IEEE Trans. Geosci. Remote Sens.*, vol. 57, no. 3, pp. 1664–1683, Mar. 2019.

[37] S. A. Buehler, J. Mendrok, P. Eriksson, A. Perrin, R. Larsson, and O. Lemke, "ARTS, the atmospheric radiative transfer simulator—Version 2.2, the planetary toolbox edition," *Geosci. Model Dev.*, vol. 11, no. 4, pp. 1537–1556, Apr. 2018.

[38] F. Chevallier, S. D. Michele, and A. McNally, "Diverse profile datasets from the ECMWF 91-level short-range forecasts," Eur. Centre Medium-Range Weather Forecasts, Reading U.K., Tech. Rep. NWPSAF-EC-TR-010, Dec. 2006.

[39] A. J. Cannon, "Quantile regression neural networks: Implementation in R and application to precipitation downscaling," *Comput. Geosci.*, vol. 37, no. 9, pp. 1277–1284, Sep. 2011.

[40] R. Koenker and K. Hallock, "Quantile regression," *J. Econ. Perspect.*, vol. 15, no. 4, pp. 143–156, 2001.

[41] S. Ioffe and C. Szegedy, "Batch normalization: Accelerating deep network training by reducing internal covariate shift," 2015, *arXiv:1502.03167*.

[42] A. Fred Agarap, "Deep learning using rectified linear units (ReLU)," 2018, *arXiv:1803.08375*.

[43] N. Srivastava, G. Hinton, A. Krizhevsky, I. Sutskever, and R. Salakhutdinov, "Dropout: A simple way to prevent neural networks from overfitting," *J. Mach. Learn. Res.*, vol. 15, pp. 1929–1958, Jun. 2014.

[44] D. P. Kingma and J. Ba, "Adam: A method for stochastic optimization," 2014, *arXiv:1412.6980*.

[45] L. Breiman, "Random forests," *Mach. Learn.*, vol. 45, no. 1, pp. 5–32, 2001.

[46] T. Chen and C. Guestrin, "XGBoost: A scalable tree boosting system," in *Proc. 22nd ACM SIGKDD Int. Conf. Knowl. Discovery Data Mining*, Aug. 2016, pp. 785–794.

[47] G. L. Ke et al., "LightGBM: A highly efficient gradient boosting decision tree," in *Proc. 31st Conf. Neural Inf. Process. Syst. (NIPS)*, Dec. 2017, pp. 1–9.

[48] B. Yong et al., "Hydrologic evaluation of multisatellite precipitation analysis standard precipitation products in basins beyond its inclined latitude band: A case study in Laohahe basin, China," *Water Resour. Res.*, vol. 46, no. 7, Jul. 2010, Art. no. W07542.

[49] C. Kummerow, "GPM GMI (GPROF) climate-based radiometer precipitation profiling L3 1 month 0.25 degree x 0.25 degree V07," Goddard Earth Sci. Data Inf. Services Center (GES DISC), Greenbelt, MD, USA, 2022, doi: 10.5067/GPM/GMI/GPROFCLIM/3A-MONTH/07.

[50] R. Pincus, P. Hubanks, and S. Platnick, "MODIS standard L3 MCD06 COSP product," Sci. Investigator-Led Process. Syst., Goddard Space Flight Center, 2020, doi: 10.5067/MODIS/MCD06COSP_M3_MODIS.061.

[51] H. Hersbach et al., "ERA5 monthly averaged data on single levels from 1940 to present," Copernicus Climate Change Service (C3S) Climate Data Store (CDS), 2023, doi: 10.24381/cds.f17050d7.

Wenyu Wang (Member, IEEE) received the B.S. degree in marine technology from the Tianjin University of Science and Technology, Tianjin, China, in 2014, the M.S. degree in physical oceanography from the National Marine Environmental Forecasting Center, Beijing, China, in 2017, and the Ph.D. degree in electromagnetic field and microwave technology from the University of Chinese Academy of Sciences, Beijing, in 2020.

He is currently an Assistant Researcher with the Key Laboratory of Microwave Remote Sensing, National Space Science Center (NSSC), Chinese Academy of Sciences (CAS), Beijing. His research interests include terahertz atmospheric sounding, retrieval method, and radiative transfer model.

Jian Xu (Senior Member, IEEE) received the B.E. degree in geographic information systems from Hohai University, Nanjing, China, in 2004, and the M.S. degree in Earth-oriented space science and technology and the Ph.D. degree in atmospheric remote sensing from Technische Universität München, Munich, Germany, in 2009 and 2015, respectively.

From 2010 to 2021, he was with the Remote Sensing Technology Institute (IMF), German Aerospace Center (DLR), Oberpfaffenhofen, Germany. He was involved in the development/refinement of atmospheric retrieval algorithms for ESA's Sentinel-5P and Sentinel-4 satellite missions. He is currently a Professor with the National Space Science Center (NSSC), Chinese Academy of Sciences (CAS), Beijing, China. His research interests include remote sensing of planetary atmosphere, radiative transfer modeling, and ill-posed inverse problems.

Husi Letu (Senior Member, IEEE) received the B.S. and M.S. degrees in geography from Inner Mongolia Normal University, Hohhot, China, in 1999 and 2002, respectively, and the Ph.D. degree in geosciences and remote sensing from the Center for Environmental Remote Sensing (CEReS), Chiba University, Chiba, Japan, in 2010.

He was with the Research and Information Center, Tokai University, Tokyo, Japan. He has been working on algorithm development and validation of the ice cloud product for JAXA's GCOM-C and Himawari-8 satellite missions. He is currently a Professor with the State Key Laboratory of the Science and Remote Sensing, Aerospace Information Research Institute (AIR), Chinese Academy of Sciences (CAS), Beijing, China. His research interests include atmospheric radiative transfer, remote sensing, simulation of the optical properties of nonspherical particles, and retrieval of ice cloud property.

Lanjie Zhang (Member, IEEE) received the Ph.D. degree in electromagnetic field and microwave technology from the National Space Science Center, Chinese Academy of Sciences, Beijing, China, in 2019.

She is currently an Associate Professor with the school of Beijing Information Science and Technology University, Beijing. Her research interests include remote sensing of sea surface salinity and sea surface wind with multifrequency microwave radiometer and scatterometer, retrieval algorithm, and applied research of atmospheric parameters.

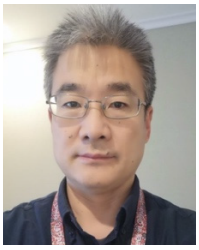

Zhenzhan Wang received the Ph.D. degree in space physics from the Graduate University, Chinese Academy of Sciences (CAS), Beijing, China, in 2005.

Since 2005, he has been a Professor with the National Space Science Center, CAS, and the Vice Director of the Key Laboratory of Microwave Remote Sensing, CAS. He hosted and participated in multiple major national research projects: ShenZhou-4, Chang'E-1/2, FengYun-3, HaiYang-2, and other satellite microwave and optical remote sensor calibration/inspection and applied research tasks. His research interests include microwave radiation measurement technology, retrieval algorithm and applied research of atmospheric and oceanic parameters, calibration technology and methods of microwave polarimetric radiometers, and mechanism and applications of atmosphere detection at terahertz.

Jiancheng Shi (Fellow, IEEE) is currently a Senior Research Scientist with the National Space Science Center, Chinese Academy of Sciences (CAS), Beijing, China. He has authored more than 500 articles with nearly 14 000 citations. His research interests mainly include remote sensing theory and techniques; remote sensing of cryosphere components, water cycle components, and radiation energy balance; development of new satellite missions; and synergy of remote sensing observations and Earth process models for hydrology and climatic change.

Dr. Shi is a fellow of Society of Photo-Optical Instrumentation Engineers (SPIE).